



Dwarf Galaxy Discoveries from the KMTNet Supernova Program. I. The NGC 2784 Galaxy Group*

Hong Soo Park^{1,2} , Dae-Sik Moon³ , Dennis Zaritsky⁴ , Mina Pak^{1,2}, Jae-Joon Lee¹ , Sang Chul Kim^{1,2},
Dong-Jin Kim¹ , and Sang-Mok Cha¹

¹ Korea Astronomy and Space Science Institute, 776, Daedeokdae-ro, Yuseong-gu, Daejeon 34055, Korea; hspark@kasi.re.kr

² Korea University of Science and Technology (UST), Daejeon 34113, Korea

³ Dept. of Astronomy and Astrophysics, University of Toronto, 50 St. George Street, Toronto, ON M5S 3H4, Canada

⁴ Steward Observatory, University of Arizona, 933 North Cherry Avenue, Tucson, AZ 85719, USA

Received 2016 December 30; revised 2017 July 12; accepted 2017 August 23; published 2017 October 5

Abstract

We present *BVI* surface photometry of 31 dwarf galaxy candidates discovered in a deep image stack from the KMTNet Supernova Program of ~ 30 square degrees centered on the nearby NGC 2784 galaxy group. Our final images have a 3σ surface brightness detection limit of $\mu_V \approx 28.5$ mag arcsec $^{-2}$. The faintest central surface brightness that we measure is $\mu_{0,V} = 26.1$ mag arcsec $^{-2}$. If these candidates are at the distance of NGC 2784, then they have absolute magnitudes greater than $M_V = -9.5$ mag and effective radii larger than 170 pc. Their radial number density decreases exponentially with distance from the center of NGC 2784 until it flattens beyond a radius of 0.5 Mpc. We interpret the baseline density level to represent the background contamination and estimate that 22 of the 31 new candidates are dwarf members of the group. The candidate's average color, $\langle(B - V)_0\rangle \approx 0.7$, and Sérsic structural parameters are consistent with those parameters for the dwarf populations of other groups. We find that the central population of dwarfs is redder and brighter than the rest of the population. The measured faint-end slope of the luminosity function, $\alpha \approx -1.33$, is steeper than that of the Local Group, but consistent with published results for other groups. Such comparisons are complicated by systematic differences among different studies, but will be simpler when the KMTNet survey, which will provide homogenous data for 15–20 groups, is completed.

Key words: galaxies: dwarf – galaxies: individual (NGC 2784)

1. Introduction

Dwarf galaxies in nearby ($D \lesssim 10$ Mpc) galaxy groups are probes of the evolution of low-mass galaxies in low-density environments. Their properties, such as the luminosity function (LF) or radial distribution within a group, are often used as tests of conventional hierarchical cosmology models. For example, one challenge to the simple standard paradigm is that the number of dwarf galaxies predicted in a Λ CDM model is much larger than that observed near the Milky Way (Klypin et al. 1999; Moore et al. 1999). Various solutions to this problem have been suggested, such as suppression of galaxy formation by photoionization (Benson et al. 2002; Cooper et al. 2010) and a steeply declining relation between stellar mass and halo mass (Behroozi et al. 2010), and the problem has lessened with the subsequent discovery of numerous faint Milky Way dwarf galaxies in surveys like the Sloan Digital Sky Survey (McConnachie 2012) and the Dark Energy Survey (Bechtol et al. 2015; Drlica-Wagner et al. 2015). Nevertheless, the apparent conflict helped focus theoretical work on aspects of the quenching of star formation in low-mass group galaxies (Presotto et al. 2012; Wetzel et al. 2012) and observational work on addressing deficits in the original data.

Several recent searches for new dwarf galaxies in nearby groups have exploited CCD cameras with wide fields of view ($\gtrsim 1$ sq. deg.). Chiboucas et al. (2009) reported 22 new dwarf galaxies found in an area of ~ 65 sq. deg. around the M81 group using CFHT/MegaCam. Müller et al. (2015) found 16 new dwarf galaxies in an area of ~ 60 sq. deg. around M83 using Dark Energy Camera at the CTIO 4 m telescope. The

same group also reported ~ 40 new dwarf galaxy candidates in the Centaurus group region (Müller et al. 2017). Other studies have explored the NGC 5128 group (Crnojević et al. 2016), the M106 group (Kim et al. 2011), the NGC 1023 group (Trentham & Tully 2009), and the M101 group (Merritt et al. 2014). These studies all discovered new dwarf galaxies, reaching as faint as $M_V \sim -10$ mag. An aim of these studies is to establish the general properties of dwarf galaxies in groups and identify any variations that depend on group properties. However, despite all of this recent progress, it is difficult to construct a coherent picture because comparing among different studies is undermined by systematic differences in data quality, selection criteria, and methodology. So motivated, we are carrying out a search for dwarf galaxies around other nearby galaxy groups using a single, large survey. We present our first results here.

The NGC 2784 group contains the lenticular-type NGC 2784 galaxy and at least 10 other galaxies (Fouque et al. 1992; Garcia 1993; Karachentsev et al. 2013). The distance measurement, 9.8 Mpc, comes from applying the surface brightness fluctuation method (Tonry et al. 2001). This galaxy group is among the fields targeted by the Korean Microlensing Telescope Network (KMTNet) Supernova Program (KSP; Moon et al. 2016), which is an international supernovae search with associated follow-up photometry using three 1.6 m telescopes. The field of view of these telescopes is extremely wide (4 sq. deg. per exposure) and we utilize the total exposure obtained over several hundreds of individual images obtained for the supernova and optical transient (He et al. 2016) search.

This paper is organized as follows. In Section 2, we describe the observations and data reduction. In Section 3, we discuss the search technique and the surface photometry of the dwarf galaxy candidates. In Section 4, we present the properties of the

* Based on data collected at KMTNet Telescopes.

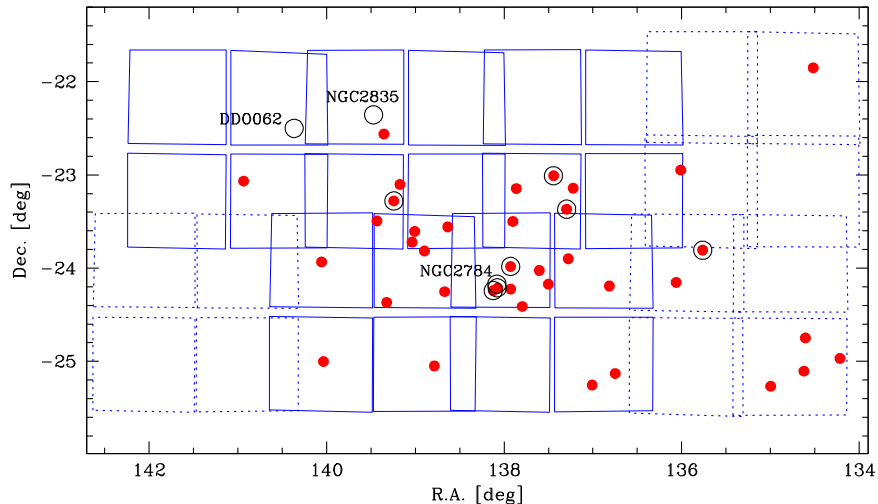


Figure 1. Finding chart for the NGC 2784 field. The filled circles are dwarf galaxy candidates of the NGC 2784 field. The open circles indicate nearby galaxies within 11 Mpc (Karachentsev et al. 2013) and we labeled three of the brightest galaxies in this field. The large solid and dotted squares indicate observed individual fields with approximately $1^\circ \times 1^\circ$ area for deep and shallow stack images, respectively.

NGC 2784 group and discuss our results in comparison to those published for other galaxy groups.

2. Observations and Data Reduction

We carried out *BVI* observations of eight fields around NGC 2784 using the KMTNet facility (Kim et al. 2016) between 2015 February and July. KMTNet is a network of three new wide-field 1.6 m telescopes, located at the Cerro Tololo Inter-American Observatory (CTIO, Chile), the South African Astronomical Observatory (SAAO, South Africa), and Siding Spring Observatory (SSO, Australia). Each telescope is equipped with a wide-field CCD camera covering 4 sq. deg. ($2^\circ \times 2^\circ$) with $0.^{\prime\prime}4$ pixel $^{-1}$ sampling. The detector is a mosaic of four 9 K \times 9 K E2V chips with a small gap between chips, and each chip corresponds to $1^\circ \times 1^\circ$ field. We used *BVI* filters and the exposure time for an individual frame was fixed to be 60 sec for any of the filters. In Figure 1, we overlay the positions of the dwarf galaxy candidates discovered in this work (see Section 3) on top of the eight observed fields. We observed five of the eight fields several hundred times through each filter and the remaining three fields only tens of times.

After pre-processing the raw images, which includes cross-talk correction, overscan subtraction, and flat fielding, we do the astrometric calibration using the *SCAMP* routine (Bertin 2006) with the GSC-2.3 reference catalog for each of the four $1^\circ \times 1^\circ$ chips. We then apply the *SWarp* routine (Bertin et al. 2002) to create deep, stacked images. At that time, to subtract the sky, we use *SWarp*'s background subtraction and a mesh size with 512 pixels. We only use images with seeing better than 2 arcsec, resulting in an average seeing for our final stacked images that is better than 1.5 arcsec in all filters. Tables 1 and 2 list the details of the fields and observations.

We derive transformation equations between instrumental magnitudes (b, v, i) and standard Johnson–Cousins magnitudes (B, V, I) using the AAVSO Photometric All-Sky Survey (APASS) catalog (APASS 2015). We use the equations as follows:

$$\begin{aligned} B &= b + c(B - V) + \text{zero}_B, \\ V &= v + \text{zero}_V, \quad I = i + \text{zero}_I. \end{aligned} \quad (1)$$

Here, c is the color coefficient and zero is the zero point magnitude for each filter. The I -band magnitude is referenced to the Sloan i -band magnitude because the APASS catalog includes only Sloan i -band magnitudes. We derive transformation equations for each chip by matching the magnitudes of bright point sources measured using SExtractor (Bertin & Arnouts 1996) to the APASS catalog. In the case of the deep image stacks, zero values are approximately 3.4, 3.4, and 3.7 mag and rms values are about 0.02, 0.02, and 0.04 mag for the B, V, I -bands, respectively. In the case of the shallow image stacks, zero values are approximately 4.0, 3.9, and 4.2 mag and rms values are about 0.03, 0.03, and 0.07 mag for the B, V, I -bands, respectively. The c color coefficient for both the deep or shallow image stacks is 0.27. The number of point sources used in the calibration is about 300 per chip. Figure 2 is an example (N2784-4-Q0 field including the NGC 2784 galaxy) of how differences in the pass bands between APASS and KMT propagate to color dependencies. The B -band only shows significant color dependency. We note that the relatively larger scatter at the I -band is caused by the different filter system between KMTNet and APASS. We correct the measured magnitudes for foreground Galactic extinction of $A_B = 0.761$, $A_V = 0.575$, and $A_i = 0.356$ ($A_I = 0.316$) (Schlafly & Finkbeiner 2011).⁵

3. Results

3.1. Searching for Dwarf Galaxy Candidates

Three of us (H. S. Park, M. Pak, and S. C. Kim) visually select dwarf galaxy candidates. We contend that visual

⁵ We pause here to clarify a variety of potentially confusing notation. First, we only apply extinction corrections to total magnitudes and colors. If such corrections have been applied, then we signify that with a subscript 0, as in $(B - V)_0$. If no subscript is included, then the corrections have not been applied. Second, for historical consistency we also use the subscript 0 to refer to central values, as in the central surface brightness, μ_0 . The subscript here does not imply that an extinction correction was applied. Third, we also use the subscript zero on a scaling radius, r_0 , that is different from the effective radius, r_e . The relationship between the scaling radius and r_e depends on the Sérsic index, n .

Table 1
Observing Log for Deep Stack Images

Field	Filter	R.A.(J2000) (hh:mm:ss)	Decl.(J2000) (dd:mm)	$T(\text{exp})$ ($N \times \text{s}$)	Date(UT) (2015.mm.dd.)	Seeing (arcsec)
N2784-3-Q0	<i>I</i>	09:10:43	-22:08	397 × 60 s	03.01.-06.30.	1.4
N2784-3-Q0	<i>V</i>	09:10:43	-22:08	383 × 60 s	03.01.-06.30.	1.5
N2784-3-Q0	<i>B</i>	09:10:43	-22:08	349 × 60 s	03.01.-06.30.	1.6
N2784-3-Q1	<i>I</i>	09:06:05	-22:08	397 × 60 s	03.01.-06.27.	1.3
N2784-3-Q1	<i>V</i>	09:06:05	-22:08	372 × 60 s	03.01.-06.30.	1.4
N2784-3-Q1	<i>B</i>	09:06:05	-22:08	345 × 60 s	03.01.-06.29.	1.5
N2784-3-Q2	<i>I</i>	09:10:44	-23:15	405 × 60 s	03.01.-06.30.	1.3
N2784-3-Q2	<i>V</i>	09:10:44	-23:15	395 × 60 s	03.01.-07.01.	1.4
N2784-3-Q2	<i>B</i>	09:10:45	-23:15	375 × 60 s	03.01.-06.30.	1.5
N2784-3-Q3	<i>I</i>	09:06:03	-23:15	390 × 60 s	03.01.-06.30.	1.3
N2784-3-Q3	<i>V</i>	09:06:03	-23:15	368 × 60 s	03.01.-06.30.	1.4
N2784-3-Q3	<i>B</i>	09:06:03	-23:15	346 × 60 s	03.01.-06.30.	1.5
N2784-4-Q0	<i>I</i>	09:12:09	-23:53	400 × 60 s	03.01.-07.03.	1.4
N2784-4-Q0	<i>V</i>	09:12:09	-23:53	375 × 60 s	03.01.-07.03.	1.5
N2784-4-Q0	<i>B</i>	09:12:09	-23:53	353 × 60 s	03.01.-07.01.	1.7
N2784-4-Q1	<i>I</i>	09:07:27	-23:53	400 × 60 s	03.01.-07.03.	1.3
N2784-4-Q1	<i>V</i>	09:07:27	-23:53	365 × 60 s	03.01.-07.03.	1.4
N2784-4-Q1	<i>B</i>	09:07:27	-23:53	350 × 60 s	03.01.-06.29.	1.5
N2784-4-Q2	<i>I</i>	09:12:10	-25:00	409 × 60 s	03.01.-07.03.	1.3
N2784-4-Q2	<i>V</i>	09:12:10	-25:00	385 × 60 s	03.01.-07.03.	1.4
N2784-4-Q2	<i>B</i>	09:12:10	-25:00	376 × 60 s	03.01.-07.03.	1.5
N2784-4-Q3	<i>I</i>	09:07:25	-25:00	394 × 60 s	03.01.-07.03.	1.3
N2784-4-Q3	<i>V</i>	09:07:25	-25:00	366 × 60 s	03.01.-07.03.	1.4
N2784-4-Q3	<i>B</i>	09:07:26	-25:00	350 × 60 s	03.01.-07.03.	1.5
N2784-5-Q0	<i>I</i>	09:18:43	-22:08	391 × 60 s	03.01.-07.01.	1.4
N2784-5-Q0	<i>V</i>	09:18:43	-22:08	361 × 60 s	03.01.-07.01.	1.5
N2784-5-Q0	<i>B</i>	09:18:43	-22:08	341 × 60 s	03.01.-07.01.	1.7
N2784-5-Q1	<i>I</i>	09:14:04	-22:08	386 × 60 s	03.01.-07.01.	1.3
N2784-5-Q1	<i>V</i>	09:14:05	-22:08	353 × 60 s	03.01.-07.01.	1.4
N2784-5-Q1	<i>B</i>	09:14:05	-22:08	331 × 60 s	03.01.-06.29.	1.5
N2784-5-Q2	<i>I</i>	09:18:44	-23:15	396 × 60 s	03.01.-07.01.	1.3
N2784-5-Q2	<i>V</i>	09:18:45	-23:15	375 × 60 s	03.01.-07.01.	1.4
N2784-5-Q2	<i>B</i>	09:18:45	-23:15	361 × 60 s	03.01.-07.01.	1.5
N2784-5-Q3	<i>I</i>	09:14:03	-23:15	383 × 60 s	03.01.-07.01.	1.3
N2784-5-Q3	<i>V</i>	09:14:03	-23:15	353 × 60 s	03.01.-07.01.	1.4
N2784-5-Q3	<i>B</i>	09:14:03	-23:15	337 × 60 s	03.01.-06.30.	1.5
N2784-6-Q0	<i>I</i>	09:20:09	-23:53	389 × 60 s	03.01.-06.30.	1.4
N2784-6-Q0	<i>V</i>	09:20:09	-23:53	361 × 60 s	03.01.-06.30.	1.5
N2784-6-Q0	<i>B</i>	09:20:09	-23:53	331 × 60 s	03.01.-06.30.	1.6
N2784-6-Q1	<i>I</i>	09:15:27	-23:53	383 × 60 s	03.01.-06.30.	1.3
N2784-6-Q1	<i>V</i>	09:15:27	-23:53	349 × 60 s	03.01.-06.30.	1.4
N2784-6-Q1	<i>B</i>	09:15:27	-23:53	328 × 60 s	03.01.-06.29.	1.5
N2784-6-Q2	<i>I</i>	09:20:10	-25:00	391 × 60 s	03.01.-06.30.	1.3
N2784-6-Q2	<i>V</i>	09:20:10	-25:00	366 × 60 s	03.01.-06.30.	1.4
N2784-6-Q2	<i>B</i>	09:20:10	-25:00	352 × 60 s	03.01.-06.30.	1.5
N2784-6-Q3	<i>I</i>	09:15:26	-25:00	377 × 60 s	03.01.-06.30.	1.3
N2784-6-Q3	<i>V</i>	09:15:25	-25:00	340 × 60 s	03.01.-06.30.	1.4
N2784-6-Q3	<i>B</i>	09:15:26	-25:00	324 × 60 s	03.01.-06.30.	1.5
N2784-7-Q0	<i>I</i>	09:26:43	-22:08	371 × 60 s	03.01.-06.29.	1.4
N2784-7-Q0	<i>V</i>	09:26:43	-22:08	346 × 60 s	03.01.-06.29.	1.5
N2784-7-Q0	<i>B</i>	09:26:43	-22:08	324 × 60 s	03.01.-06.29.	1.7
N2784-7-Q1	<i>I</i>	09:22:05	-22:08	371 × 60 s	03.01.-06.29.	1.3
N2784-7-Q1	<i>V</i>	09:22:05	-22:08	334 × 60 s	03.01.-06.29.	1.4
N2784-7-Q1	<i>B</i>	09:22:05	-22:08	317 × 60 s	03.01.-06.26.	1.6
N2784-7-Q2	<i>I</i>	09:26:45	-23:15	372 × 60 s	03.01.-06.29.	1.3
N2784-7-Q2	<i>V</i>	09:26:45	-23:15	352 × 60 s	03.01.-06.29.	1.4
N2784-7-Q2	<i>B</i>	09:26:45	-23:15	344 × 60 s	03.01.-06.29.	1.5
N2784-7-Q3	<i>I</i>	09:22:03	-23:15	363 × 60 s	03.01.-06.29.	1.3
N2784-7-Q3	<i>V</i>	09:22:03	-23:15	330 × 60 s	03.01.-06.29.	1.4
N2784-7-Q3	<i>B</i>	09:22:03	-23:15	316 × 60 s	03.01.-06.29.	1.5

Table 2
Observing Log for Shallow Stack Images

Field	Filter	R.A.(J2000) (hh:mm:ss)	Decl.(J2000) (dd:mm)	$T(\text{exp})$ ($N \times \text{s}$)	Date(UT) (2015.mm.dd.)	Seeing (arcsec)
N2784-1-Q0	<i>I</i>	09:03:22	-21:56	8 × 100 s	02.09.-02.27.	1.3
N2784-1-Q0	<i>V</i>	09:03:22	-21:56	7 × 100 s	02.09.-02.27.	1.2
N2784-1-Q0	<i>B</i>	09:03:22	-21:56	6 × 100 s	02.09.-02.27.	1.4
N2784-1-Q1	<i>I</i>	08:58:44	-21:56	8 × 100 s	02.09.-02.27.	1.3
N2784-1-Q1	<i>V</i>	08:58:44	-21:56	7 × 100 s	02.09.-02.27.	1.2
N2784-1-Q1	<i>B</i>	08:58:44	-21:56	8 × 100 s	02.09.-02.27.	1.5
N2784-1-Q2	<i>I</i>	09:03:23	-23:03	8 × 100 s	02.09.-02.27.	1.2
N2784-1-Q2	<i>V</i>	09:03:23	-23:03	7 × 100 s	02.09.-02.27.	1.2
N2784-1-Q2	<i>B</i>	09:03:23	-23:03	6 × 100 s	02.09.-02.27.	1.2
N2784-1-Q3	<i>I</i>	08:58:42	-23:03	8 × 100 s	02.09.-02.27.	1.2
N2784-1-Q3	<i>V</i>	08:58:43	-23:03	7 × 100 s	02.09.-02.27.	1.2
N2784-1-Q3	<i>B</i>	08:58:43	-23:03	6 × 100 s	02.09.-02.27.	1.3
N2784-2-Q0	<i>I</i>	09:03:24	-23:56	5 × 100 s	02.09.-02.27.	1.0
N2784-2-Q0	<i>V</i>	09:03:24	-23:56	5 × 100 s	02.09.-02.27.	1.2
N2784-2-Q0	<i>B</i>	09:03:24	-23:56	5 × 100 s	02.09.-02.27.	1.2
N2784-2-Q1	<i>I</i>	08:58:42	-23:56	5 × 100 s	02.09.-02.27.	1.1
N2784-2-Q1	<i>V</i>	08:58:42	-23:56	5 × 100 s	02.09.-02.27.	1.2
N2784-2-Q1	<i>B</i>	08:58:42	-23:56	4 × 100 s	02.09.-02.27.	1.3
N2784-2-Q2	<i>I</i>	09:03:25	-25:03	5 × 100 s	02.09.-02.27.	1.0
N2784-2-Q2	<i>V</i>	09:03:25	-25:03	5 × 100 s	02.09.-02.27.	1.2
N2784-2-Q2	<i>B</i>	09:03:26	-25:03	5 × 100 s	02.09.-02.27.	1.2
N2784-2-Q3	<i>I</i>	08:58:40	-25:03	5 × 100 s	02.09.-02.27.	1.1
N2784-2-Q3	<i>V</i>	08:58:40	-25:03	5 × 100 s	02.09.-02.27.	1.2
N2784-2-Q3	<i>B</i>	08:58:40	-25:03	5 × 100 s	02.09.-02.27.	1.3
N2784-8-Q0	<i>I</i>	09:28:09	-23:53	4 × 100 s	02.11.-02.15.	1.1
N2784-8-Q0	<i>V</i>	09:28:09	-23:53	3 × 100 s	02.11.-02.15.	1.1
N2784-8-Q0	<i>B</i>	09:28:09	-23:53	4 × 100 s	02.11.-02.15.	1.3
N2784-8-Q1	<i>I</i>	09:23:27	-23:53	4 × 100 s	02.11.-02.15.	1.1
N2784-8-Q1	<i>V</i>	09:23:27	-23:53	3 × 100 s	02.11.-02.15.	1.1
N2784-8-Q1	<i>B</i>	09:23:27	-23:53	4 × 100 s	02.11.-02.15.	1.3
N2784-8-Q2	<i>I</i>	09:28:10	-25:00	4 × 100 s	02.11.-02.15.	1.3
N2784-8-Q2	<i>V</i>	09:28:10	-25:00	3 × 100 s	02.11.-02.15.	1.1
N2784-8-Q2	<i>B</i>	09:28:10	-25:00	4 × 100 s	02.11.-02.15.	1.3
N2784-8-Q3	<i>I</i>	09:23:25	-25:00	4 × 100 s	02.11.-02.15.	1.2
N2784-8-Q3	<i>V</i>	09:23:25	-25:00	3 × 100 s	02.11.-02.15.	1.1
N2784-8-Q3	<i>B</i>	09:23:26	-25:00	4 × 100 s	02.11.-02.15.	1.3

identification is more complete and less contaminated than current automatic detection methods (Kim et al. 2011; Müller et al. 2015). Our selection criteria, applied to images displayed using the zscale option in *DS9*, are that (1) there must be a diffuse stellar component that extends at least ~ 10 arcsec, (2) the object must not exhibit any distinct structure (e.g., such as spiral structure) except for a possible nuclear point source, and (3) the object must not have a steep surface brightness gradient between the center and the edge, such as that expected for luminous background galaxies. Our selection is mainly based on the *I*-band images, but we use the *B* and *V*-band images as well as the RGB color images made from the three bands to rule out artifacts. HSP, MP, and SCK searched the images independently and then compared results. For the targets selected by only one or two classifiers, all three classifiers reviewed the object and reached a consensus on whether to retain or reject the candidate.

We visually inspect each chip in each of the eight NGC 2784 fields, including both the shallow and deep image stacks. We detect 38 objects that we classify as dwarf galaxy candidates and plot their positions in Figure 1. There are seven previously identified dwarf candidates in the NGC 2784 fields (Karachentsev et al. 2013). We recover all of them. Three (ESO497-004, DDO056, and HIPASS J0916-23b) of these have been

spectroscopically confirmed to be members (Fisher & Tully 1981; Doyle et al. 2005; Karachentsev et al. 2008), while the other four (KK71, KK72, NGC 2784 dw01, KK73) await spectroscopic confirmation. In addition, the group also contains three brighter galaxies (NGC 2784, NGC 2835, and DDO062) that have been spectroscopically confirmed as members. We present *I*-band grayscale images of all the dwarf galaxy candidates in Figures 3. Many of the images have evident vertical lines, which are due to charge bleeds or blooming caused by saturation of the bright foreground stars on the CCD images. These artifacts do not affect our candidate detection because the sources are more extended nor do they affect our surface photometry because we mask the artifacts (see Section 3.2). The candidates exhibit a range of morphologies and sizes, and sometimes have an evident unresolved nuclear source.

We test our completeness and limiting brightness by inserting artificial sources in the images. We adopt exponential surface brightness ($n = 1$) profiles and central brightness and effective radii distributions that reproduce the effective radius-magnitude trend of our NGC 2784 dwarf candidates (Figure 7 and Section 3.5). We insert several hundred artificial galaxies in the *I*-band image that includes NGC 2784 using the mkobjects task in the IRAF/artdata package. We then reapply our visual inspection technique. We find that for $m_i = 18.9$

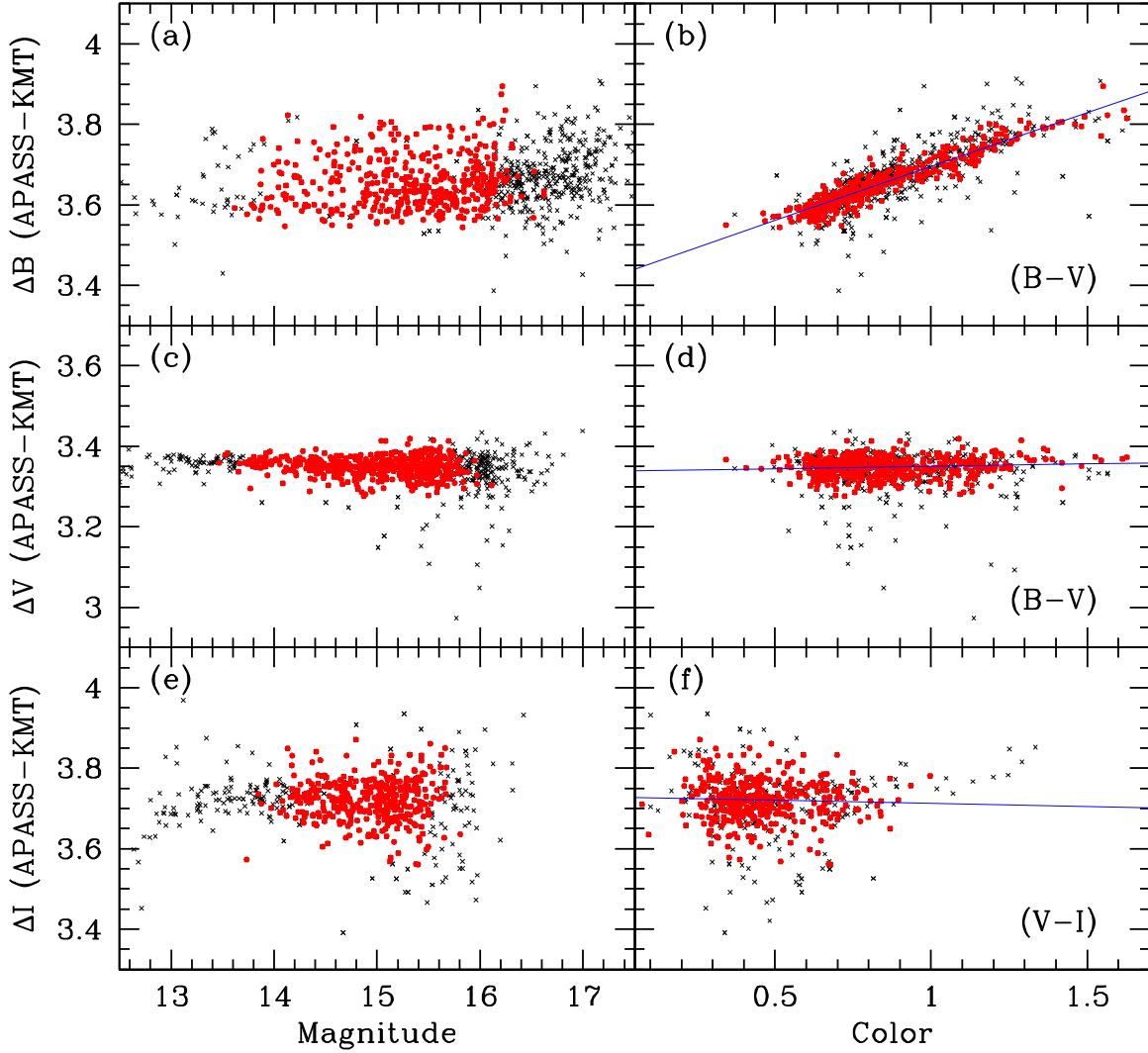


Figure 2. Magnitude difference between APASS standard magnitude and KMTNet instrumental magnitude as a function of magnitude (left panels) and color (right panels). The data with the red filled circles and black crosses are the point sources matched between APASS catalog and KMTNet photometry catalog. The solid lines represent the linear least-square fits to the red filled circles, which indicate the data within 3σ from the fits with too bright or too faint stars are excluded.

($M_V = -11.0$ at the distance of NGC 2784) we are 90% complete. The last thumbnail image in Figure 3 contains an artificial dwarf galaxy at this magnitude limit ($m_I = 18.9$ mag and $r_e = 17.5$ pixel). Several studies have shown that the surface brightness of dwarf galaxies can be described by a Sérsic profile and their Sérsic index distribution is peaked around $n \approx 0.7$ (Ferrarese et al. 2006; Muñoz et al. 2015). Thus, we also carry out the completeness test with $n = 0.7$. We find that for $m_I = 19.1$ ($M_V = -10.8$) we are 90% complete. We present detections down to $M_V \sim -10$, so we expect to be significantly incomplete at our limiting magnitude. In addition, our completeness simulations do not account for other possible populations. For example, we do not include ultra compact dwarf galaxies that we might have considered to be stars or background galaxies. Therefore, the number 38 is a lower limit on the number of the dwarf candidates in these fields.

3.2. Surface Photometry

We measure the surface brightness profiles of the 38 dwarf candidates in B , V , I using the IRAF/ellipse task. We fix the center coordinates, ellipticities, and position angles, which we

estimate near the effective radius of each candidate. We use linear semimajor axis steps of 1.0 arcsec for the smaller candidates and 1.5 arcsec for the larger ones. The brightness of each isophote is measured from mean isophotal flux, and its error is the root mean square scatter of the isophotal flux values. The instrumental brightnesses obtained from this surface photometry are transformed using the transformation equations (Equation (1) in Section 2).

We present the surface brightness and color profiles in Figure 4. Most candidate have surface brightness profiles that are well described as exponential ($n \sim 1$) and have constant color profiles. The 3σ faintest surface brightnesses reached on our shallow and deep image stacks are $\sim \mu_I \approx 26.5$ ($\mu_V \sim 26.9$) mag arcsec $^{-2}$ and $\mu_I \sim 28.0$ ($\mu_V \sim 28.5$) mag arcsec $^{-2}$, respectively. In the color profile panels, the dotted-dashed line represents the weighted mean value. We adopt these mean values ($\langle \mu_{(V-I)} \rangle$ and $\langle \mu_{(B-V)} \rangle$) as the colors ($(V-I)$ and $(B-V)$) of the dwarf candidates. The total magnitudes are estimated from the extrapolation of a fitted brightness profile, and B -band signal is relatively much shallower due to same exposure time in each band (B , V , I). Thus, in this study, the mean value from brightness profiles is more efficient for

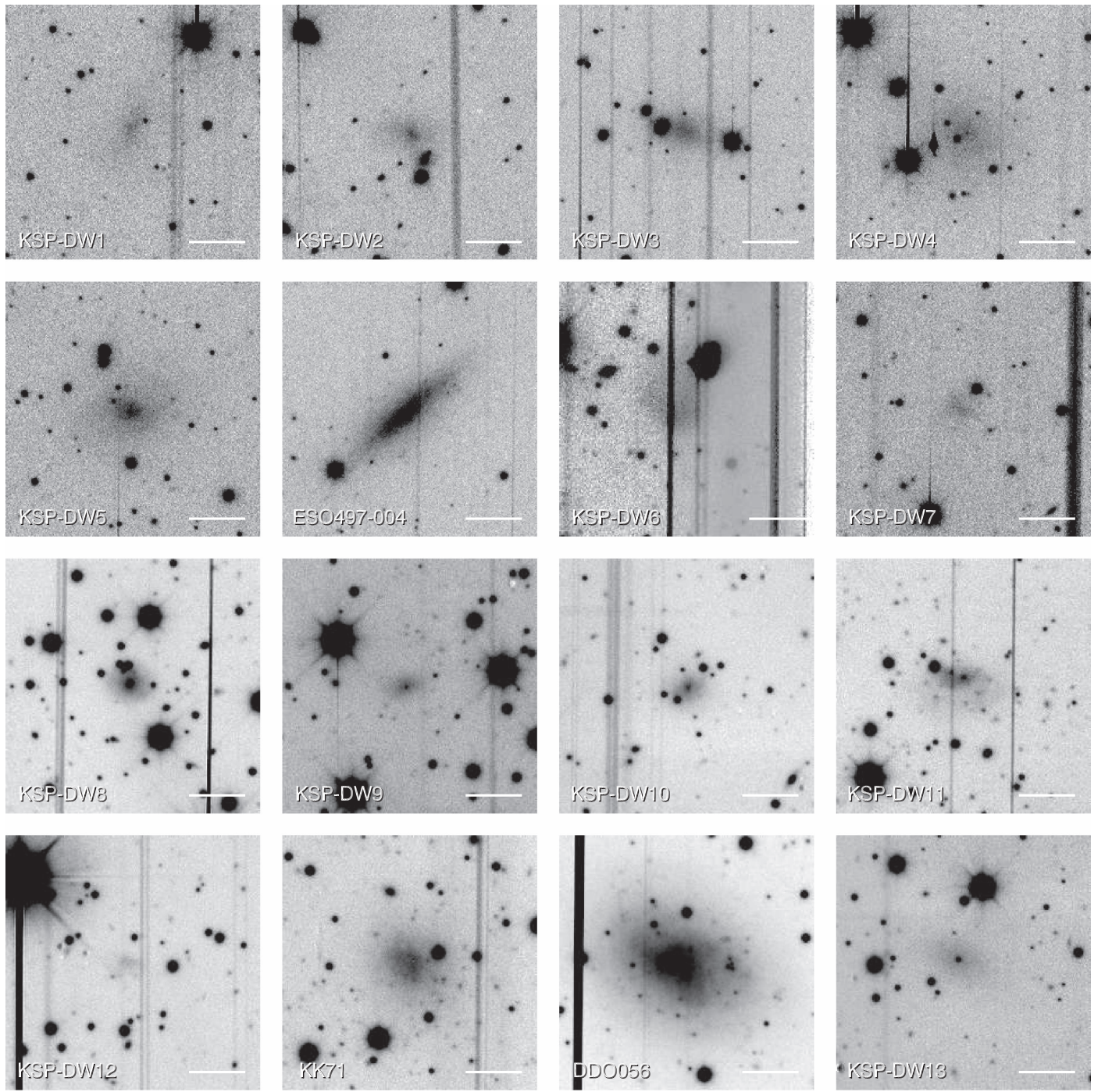


Figure 3. I -band images of the dwarf galaxy candidates. The scale bar in each panel represents 20 arcsec, and the field of view of most images is approximately 1.5 arcmin \times 1.5 arcmin. The last thumbnail figure represents an artificial dwarf galaxy around the brightness with about 90% completeness. North is up, east is left.

representing the color of each dwarf. The color ranges are $0.6 < (B - V) < 1.2$ and $0.3 < (V - I) < 1.2$.

We fit Sérsic functions ($\mu_0 + 1.0857(r/r_0)^{1/n}$) to the surface brightness profiles, where μ_0 , r_0 , and n are the central surface brightness, scale length, and Sérsic curvature index, respectively. We adopt the 1-sigma statistical errors computed from the nonlinear least squares fitting procedure (Markwardt 2009) as the errors for the Sérsic parameters. We show these fits with solid curves in Figure 4. As a test, we compare the profiles of the dwarf candidates that were observed in overlapping images (Figure 1). The resulting profile parameters are statistically

consistent. The faintest central surface brightnesses among the dwarf candidates are $\mu_{0,I} \sim 25.1$, $\mu_{0,V} \sim 26.1$, and $\mu_{0,B} \sim 26.9$ mag arcsec $^{-2}$. The Sérsic scale lengths range from $2 < r_{0,I} < 23$ arcsec, and the curvature indices from $0.5 < n_I < 1.4$, with median value of ~ 0.8 . The total magnitudes of the dwarf candidates using these fits, following the method described in Section 3.1 of Chiboucas et al. (2009), result in the faintest I_T , V_T , and B_T being ~ 20.5 , 20.6, and 21.7 mag, respectively. The smallest I -band effective radius ($r_{e,I}$) is ~ 3.5 arcsec (corresponding to ~ 170 pc at the distance of NGC 2784).

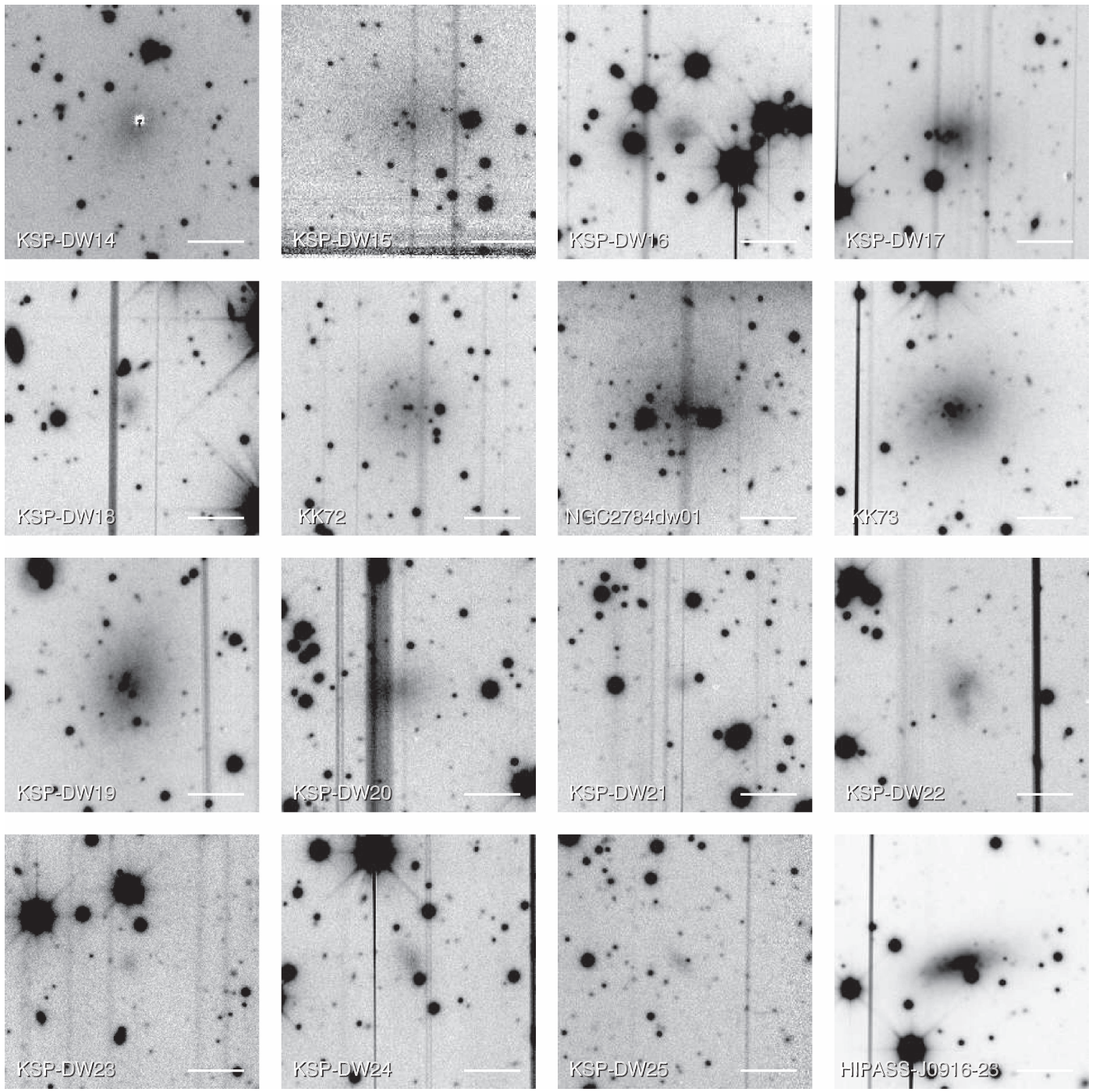


Figure 3. (Continued.)

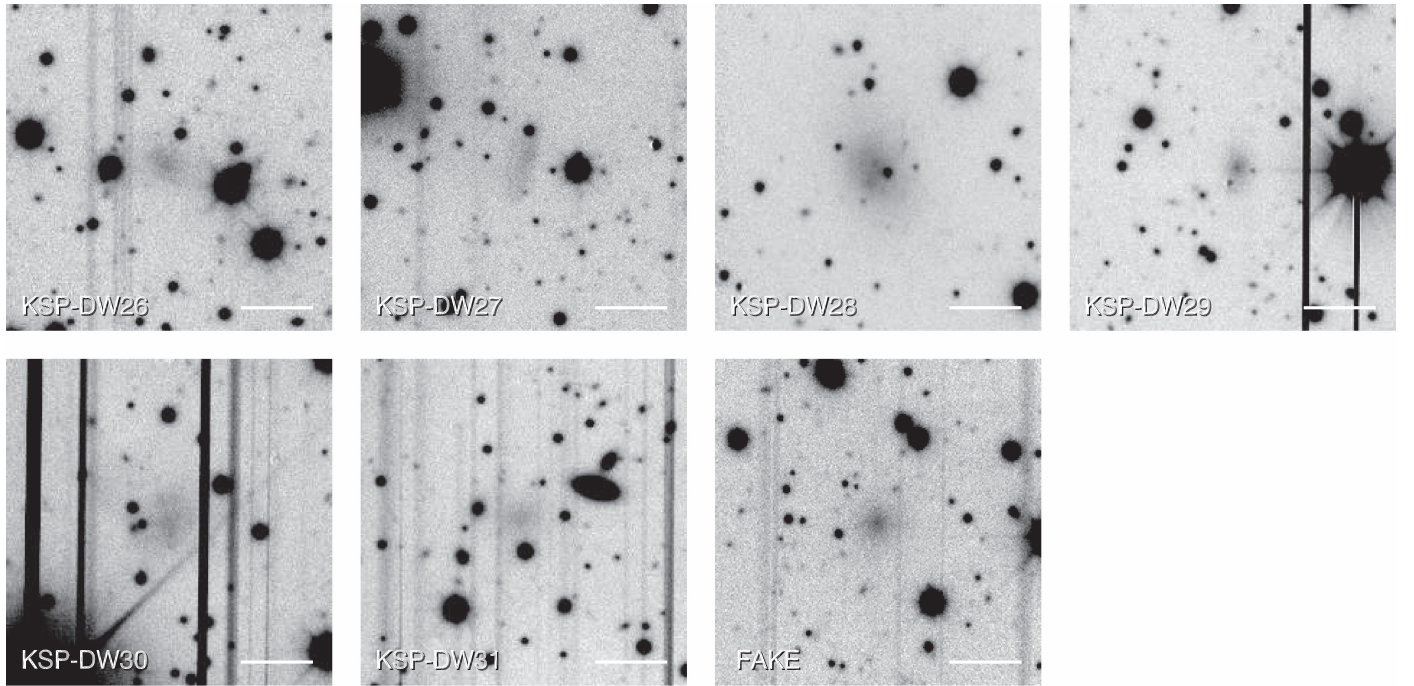
3.3. The NGC 2784 Dwarf Galaxy Catalog

We present the photometric catalog for the 38 dwarf candidates in Table 3. The first column contains our identification or the previously established galaxy name if available (Karachentsev et al. 2013). The second and third columns have the central R.A. (J2000) and decl. (J2000). The fourth column presents the I -band total magnitude derived from the Sérsic fit result. The fifth and the sixth columns list the $(V - I)$ and $(B - V)$ colors, respectively. Because the Galactic extinction values toward NGC 2784 depend on an adopted extinction map or calibration, we present the colors without the

extinction correction. The seventh, eighth, and ninth columns contain the central surface brightness ($\mu_{0,I}$), scale length ($r_{0,I}$), and curvature index (n_I) derived for the Sérsic fit, respectively. The I -band $r_{e,I}$ as derived from our fits is in the tenth column. We could not reliably measure $(B - V)$ for KSP-DW6, and $(V - I)$ and $(B - V)$ for KSP-DW23, due to the low surface brightness of these galaxies.

3.4. Radial Number Density

We present the number density of dwarf candidates in the NGC 2784 field as a function of the projected radius (R) from

**Figure 3.** (Continued.)

the center of the stellar light of NGC 2784 in Figure 5. Here, we carefully estimate the unit “projected area” due to complex survey coverage (e.g., overlapped area, rectangular coverage on the whole) as seen in Figure 1, and we adopt density errors assuming a Poisson distribution. The number density, obtained from the visually identified dwarfs only in the region covered by deep stack images, decreases outwardly until the last bin ($3 \lesssim R \lesssim 4$ degree) where it flattens. We interpret the baseline flat level as an indication that we have reached the background density of objects that satisfy our selection criteria. It is possible that the profile of true dwarfs flattens somewhat at large radii, but conservatively we interpret this as the contamination level. In contrast, when we examine the density profile using the region covered by shallow and deep stacks, it rises at the outermost bin even though we expect the shallow stacks to be more incomplete. However, most objects in this bin are concentrated in the south–west region and located at $R \gtrsim 3$ degree from the NGC 2784. We suspect that these candidates are contaminants.

When we fit the density distribution from only the deep stack results with an exponential profile plus a constant value, we find that the surface density (Σ) is described by $\Sigma = e^{-1.62(\pm 0.19)R + 2.52(\pm 0.29)} + 0.24(\pm 0.12)$. The constant value (0.24 deg^{-2}) is the contamination level. The density profile is also well described by a power law with equal logarithmic interval (Figure 5(b)). That fit has $\Sigma = 1.69(\pm 0.47)R^{-1.27(\pm 0.17)} + 0.24$. This power index ($\alpha = -1.27 \pm 0.17$) is consistent with the power index ($\alpha = -1.03 \pm 0.19$) obtained from an equal linear interval. Integrating this exponential fit and comparing the number of dwarf candidates that are radially clustered about NGC 2784 to those that are not suggests that 15% (5) of the 32 candidates within $R = 2.7$ degree are not dwarfs associated with NGC 2784. Additionally, six ($R > 2.7$ degree) out of the 38 dwarf candidates may also be not associated with NGC 2784.

3.5. Comparison with Dwarf Galaxies in Other Systems

In Figure 6, we present the color–magnitude diagram for the candidate dwarf population of NGC 2784. The mean values of $(B - V)_0$ and $(V - I)_0$, which are corrected the Galactic extinction, are 0.67 ± 0.16 and 0.45 ± 0.20 , respectively. The $(B - V)_0$ mean color is similar to those for the M106 ($\langle(B - V)_0\rangle \approx 0.73$; Kim et al. 2011) and the M83 groups ($\langle(B - V)_0\rangle \approx 0.82$; Müller et al. 2015). For comparison, we overlay the values of dwarf galaxies in other groups (M83 from Müller et al. 2015, M106 from Kim et al. 2011) and the color–magnitude relations of the early-type galaxies in clusters (Virgo from Lisker et al. 2008, and Ursa Major from Pak et al. 2014). We conclude that the color distributions are consistent and that the NGC 2784 dwarfs are mostly early-type galaxies.

We now compare the central surface brightnesses (μ_0), effective radii (r_e), and Sérsic n indices of the NGC 2784 dwarf candidates with those of dwarf galaxies in other groups. For the central surface brightnesses and effective radii we use values from Müller et al. (2015) for the M83 group and from McConnachie (2012) for the Local Group. For n , we use values from Chiboucas et al. (2009) for the M81 group, from Müller et al. (2015) for the M83 group, and from Jerjen et al. (2000) for the Local Group. For our values, we calculate $\mu_{0,V}$ and M_V using $\mu_{0,I}$ and M_I in combination with the $(V - I)$ color. We adopt $(V - I) = 0.7$ for KSP-DW23. The values for r_e and n are the values obtained from the I -band images. We assume all of the candidates are at the distance of NGC 2784. In Figure 7 we compare $\mu_{0,V}$, r_e , and n as a function M_V . The properties of the NGC 2784 dwarf candidates, with central surface brightness and effective radius increasing as the total brightness increases, agree well with the trends of the dwarfs in the M83 group and the Local Group. These results support the contention that the candidates are mostly member galaxies of the NGC 2784 group rather than background galaxies. Additionally, the median value of the Sérsic curvature index for the NGC 2784 dwarf candidates ($n \approx 0.8 \pm 0.1$) is similar

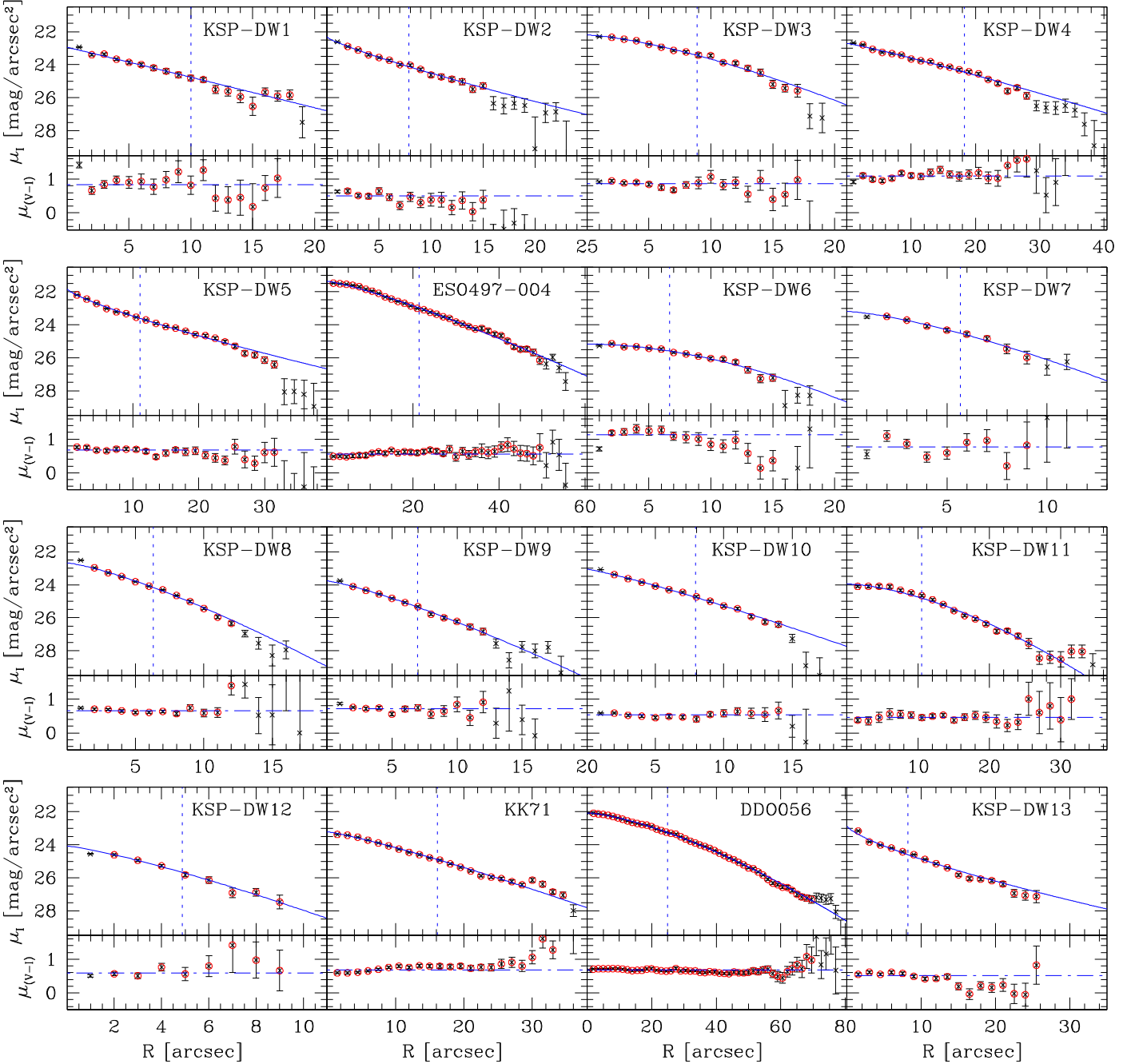


Figure 4. Surface brightness and color profiles of the dwarf candidates. The open circles in each panel indicate surface brightnesses and colors above approximately 3 sigma sky level. They are used for Sérsic fit and mean color estimation represented by the solid and dotted-dashed lines, respectively. The vertical dotted lines represent effective radius.

to that of the dwarfs in the M83 group ($n \approx 1.1 \pm 0.3$), the M81 group ($n \approx 0.6 \pm 0.2$), and the Local Group ($n \approx 1.2 \pm 0.3$). Again, the properties of the NGC 2784 candidates are entirely consistent with those of dwarfs in other groups.

4. Discussion

4.1. The NGC 2784 Galaxy Group

In Figure 8, we show the radial number density profiles of the bright ($M_V < -13$) and faint ($M_V \geq -13$) dwarf galaxy candidates in the NGC 2784 field. We fit each profile with an exponential function for $R \lesssim 2^{\circ}5$. We find that the density profile

of the brighter dwarfs ($\ln(\Sigma) = -1.63(\pm 0.19)R + 1.78(\pm 0.24)$ (rms = 0.21)) is steeper than that of the fainter dwarfs ($\ln(\Sigma) = -0.68(\pm 0.24)R + 1.18(\pm 0.31)$ (rms = 0.26)). A complication in interpreting this result is that background contamination may be distorting the fits. Although a magnitude dependent contamination is expected, our sample is too small for us to determine whether the background contamination is more significant for fainter candidates. If it is, however, it could be making the fainter population appear more extended. To test for such an effect, we added the entire fitted background level (0.24 deg^{-2} , see Section 3.4) to the density profile of the brighter galaxies. The new slope for this population is now -1.28 ± 0.19 , which is still steeper than that of the faint galaxies. We conclude, with some caution, that the

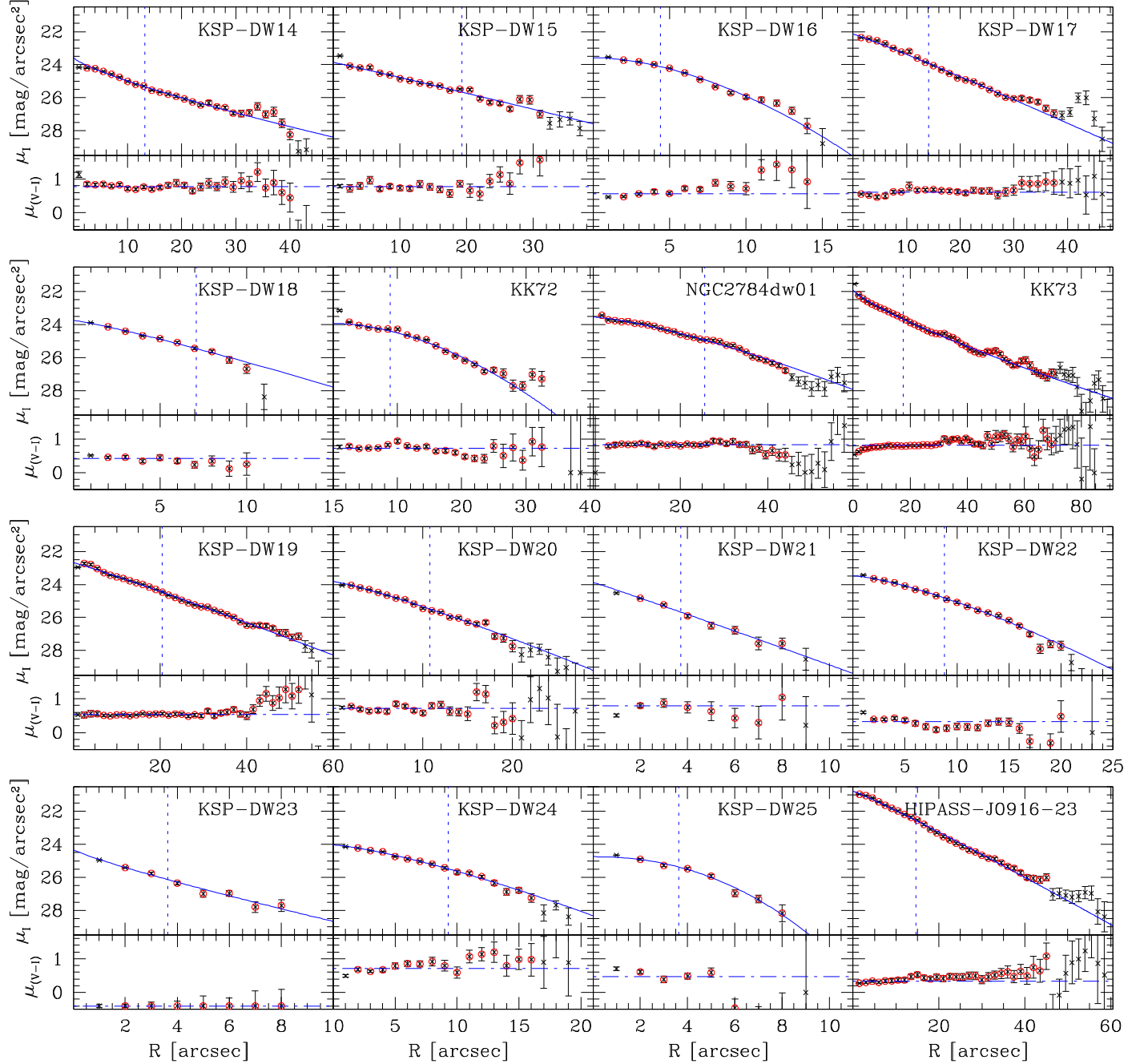


Figure 4. (Continued.)

brighter set of dwarf galaxies is more centrally concentrated. This conclusion is further supported by the results of a Z-test comparison of the radial distance distributions of the dwarf candidates within $R = 2.5$. Z-test is a statistical test to examine whether or not two samples are different population under assuming a normal distribution (Sprinthal 2011). We find with 99.1% confidence that the samples do not have the same radial distribution. The difference in central concentration may reflect mass segregation, with more massive galaxies in a cluster or group being more centrally concentrated (Presotto et al. 2012; Roberts et al. 2015). Plausible physical reasons for that apparent concentration range from environmentally dependent formation histories, differences in dynamical friction, or mass-dependent tidal stripping.

Next, we check whether there are radial variations in the mean colors of the dwarf candidates. In Figure 9, we show that the dwarfs are redder when closer to the center. The trend is also visible for bright and faint dwarfs independently. The radial fraction of red dwarf galaxies is higher in the center than in the outskirts when we estimate the red dwarf fraction using the color-magnitude relation (Equation (1)) by Weinmann et al. (2011). This observation is consistent with the results of simulations (Wetzel et al. 2012, 2013) and other observations (Popesso et al. 2006; Presotto et al. 2012; Lee et al. 2016). The standard interpretation of this effect is that the central galaxies have lower star formation rates.

This result has also been reported in galaxy clusters such as Virgo and Coma (Weinmann et al. 2011; Smith et al. 2012; Lisker et al. 2013). It is suggested that the galaxies in the

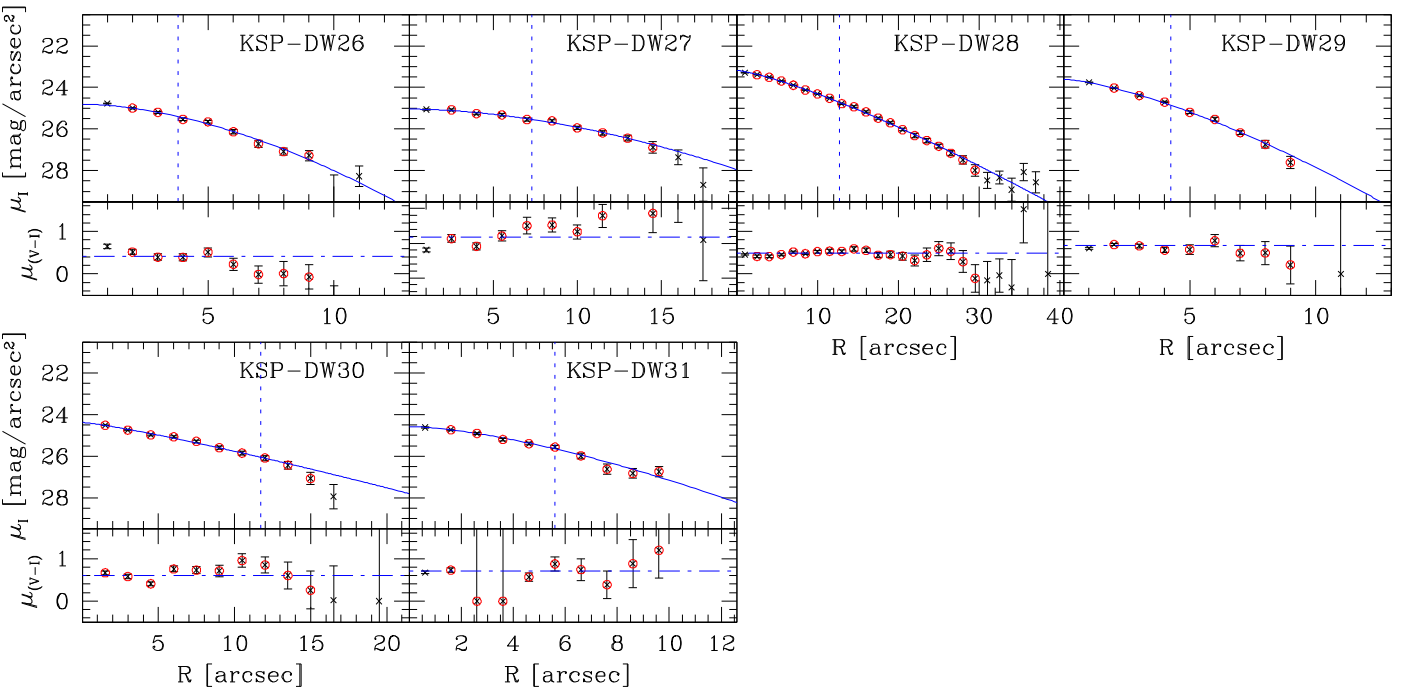


Figure 4. (Continued.)

central regions of massive clusters experienced earlier, more efficient star formation quenching due to stronger tidal forces and interactions with the intracluster medium, so the red galaxies are more centrally concentrated. The same environmental effect could be the reason for color distribution in the NGC 2784 group. On the other hand, this reddening of galaxies toward the center might also be a metallicity effect. If, as discussed above, the central galaxies are more massive than they are likely to also be more metal-rich and therefore redder. However, again this result might be influenced by differential background contamination. In general, background contaminants tend to be blue galaxies, which are more common than red galaxies, and tend to be found at larger separations due to the greater amount of sky at larger separations. This effect could result in creating a color gradient in the sense of that observed. To test for such an effect, we assume that the five dwarf candidates (this number is based on the 15% contamination rate with $R \lesssim 2.7$ degree (see Section 3.4)) are all contaminants with bluish color and we remove them from our sample. The color trend remains.

4.2. Cumulative LFs of Galaxy Groups

To investigate the LF of galaxies in the NGC 2784 group and compare it to that of galaxies in other groups, we construct the cumulative LF of the NGC 2784 group. We focus on the cumulative LF, instead of the differential LF, because the number of galaxies in each group is small (Trentham & Tully 2009). For the fainter galaxies ($M_V > -17$) in the NGC 2784 group, we use the results from the surface photometry in Table 3. For the three bright group galaxies, we also use the photometry obtained from our deep stack images: NGC 2784 ($M_V = -20.85$), NGC 2835 ($M_V = -20.44$), and DDO062 ($M_V = -17.83$). These values are consistent to within 0.4 mag with the published total absolute magnitudes (Karachentsev et al.

2013). Because of increased contamination at larger projected radii, we use only the dwarf candidates within $R < 0.5$ Mpc.

To obtain the comparison LFs, we use photometry from the literature (for the NGC 5128 group from Tully et al. 2015 and Crnojević et al. 2016; the M81 group from Chiboucas et al. 2009; for the M83 group from Müller et al. 2015; for the M106 group from Kim et al. 2011, and for the Local Group from McConnachie 2012 and Martin et al. 2013a, 2013b). Where necessary, we transform magnitudes using $M_V = M_B - 0.7$, $M_V = M_r + 0.2$ (Müller et al. 2015), and $V = g - 0.5784(g - r) - 0.0038$ (Lupton 2005).

In Figure 10, we compare the cumulative LFs of six galaxy groups, including the NGC 2784 group. We fit cumulative Schechter functions (Schechter 1976) to the observed cumulative LFs according to the method described in Section 3.2 of Chiboucas et al. (2009). The faint-end slopes (α) of the fitted cumulative LFs have values ranging from $\alpha \approx -1.0$ to $\alpha \approx -1.4$ (Table 4). The slope ($\alpha = -1.33 \pm 0.05$) for the NGC 2784 group is similar to those of the M81, M83, M106, and NGC 5218 groups, while the slope is steeper than that of the Local Group ($\alpha \approx -1.05$, which is consistent with the values from other studies Chiboucas et al. 2009; McConnachie et al. 2009; Kim et al. 2011). The slopes for the NGC 2784 group and the other five groups are much flatter than the slope ($\alpha = -1.8$) of the subhalo mass function in the Λ CDM model (Trentham & Tully 2002), shown as the dotted line in Figure 10. We also check any dependency between the faint-end slope (α) and the characteristic absolute magnitude (M^*) of the LF in each group. The α values of six groups including the NGC 2784 group change slightly ($\lesssim 30\%$) within their uncertainties (e.g., as shown in Figure 30 by Chiboucas et al. 2009, Figure 16 by Trentham & Tully 2009, and Figure 13 by Ferrarese et al. 2016). Thus the M^* is unlikely to affect significantly the α values estimated in this study.

We fit only over the magnitude range $M_V < -10$ mag. We set the faint limit at a magnitude where we are still highly

Table 3
Photometric Catalog for Dwarf Galaxy Candidates in N2784 Field

ID ^a	R.A.(J2000) (hh:mm:ss)	Decl.(J2000) (dd:mm:ss)	<i>I</i> ^b (mag)	(<i>V</i> − <i>I</i>) ^c (mag)	(<i>B</i> − <i>V</i>) ^c (mag)	$\mu_{0,I}^d$ (mag arcsec ^{−2})	$r_{0,I}^d$ (arcsec)	n_I^d	$r_{e,I}^d$ (arcsec)
KSP-DW1	08:56:52.2	−24:58:05	17.07	0.84	0.75	22.95 ± 0.16	6.05 ± 1.01	0.98 ± 0.14	10.00
KSP-DW2	08:58:04.3	−21:51:02	16.72	0.50	0.93	22.32 ± 0.15	4.29 ± 0.79	1.20 ± 0.15	7.87
KSP-DW3	08:58:25.5	−24:44:55	16.17	0.87	0.91	22.20 ± 0.03	8.14 ± 0.24	0.69 ± 0.04	8.88
KSP-DW4	08:58:29.5	−25:06:18	15.52	1.09	0.83	22.71 ± 0.06	11.98 ± 0.68	0.90 ± 0.06	18.32
KSP-DW5	08:59:59.3	−25:16:02	15.38	0.68	0.87	21.84 ± 0.04	5.95 ± 0.35	1.27 ± 0.05	11.11
ESO497-004	09:03:03.1	−23:48:24	13.75	0.56	0.74	21.36 ± 0.01	15.44 ± 0.23	0.82 ± 0.01	21.47
KSP-DW6	09:04:02.4	−22:56:52	18.66	1.13	...	25.16 ± 0.04	11.04 ± 0.32	0.54 ± 0.06	6.69
KSP-DW7	09:04:14.7	−24:09:11	18.23	0.78	0.61	23.19 ± 0.21	4.92 ± 0.82	0.72 ± 0.19	5.66
KSP-DW8	09:06:59.6	−25:07:50	17.62	0.66	0.79	22.68 ± 0.04	4.94 ± 0.17	0.77 ± 0.03	6.32
KSP-DW9	09:07:15.3	−24:11:30	18.58	0.72	0.94	23.77 ± 0.05	5.14 ± 0.26	0.80 ± 0.05	6.98
KSP-DW10	09:08:01.9	−25:15:18	17.66	0.53	0.71	23.06 ± 0.05	5.39 ± 0.26	0.86 ± 0.04	7.93
KSP-DW11	09:08:53.3	−23:08:33	17.15	0.46	0.71	23.96 ± 0.04	12.18 ± 0.34	0.62 ± 0.02	10.49
KSP-DW12	09:09:06.4	−23:53:58	19.67	0.58	0.74	24.07 ± 0.21	3.56 ± 0.65	0.81 ± 0.15	4.87
KK71	09:09:10.9	−23:22:01	16.26	0.68	0.94	23.22 ± 0.02	11.12 ± 0.18	0.85 ± 0.02	16.15
DDO056	09:09:45.9	−23:00:30	13.76	0.68	0.87	22.07 ± 0.01	23.43 ± 0.12	0.69 ± 0.00	24.96
KSP-DW13	09:10:00.0	−24:10:19	16.85	0.52	1.09	22.86 ± 0.07	4.30 ± 0.39	1.37 ± 0.07	8.17
KSP-DW14	09:10:25.0	−24:01:30	16.69	0.78	0.97	23.56 ± 0.07	7.03 ± 0.58	1.29 ± 0.06	13.19
KSP-DW15	09:11:10.7	−24:24:41	16.56	0.77	1.06	23.86 ± 0.09	11.78 ± 1.02	0.97 ± 0.08	19.28
KSP-DW16	09:11:26.9	−23:08:44	18.20	0.56	0.77	23.57 ± 0.02	6.48 ± 0.12	0.57 ± 0.02	4.41
KSP-DW17	09:11:36.2	−23:30:00	15.52	0.61	0.88	22.14 ± 0.02	8.86 ± 0.19	0.94 ± 0.02	14.14
KSP-DW18	09:11:42.2	−24:13:29	18.59	0.42	0.80	23.75 ± 0.10	4.79 ± 0.48	0.87 ± 0.11	7.10
KK72	09:11:42.4	−23:58:56	16.88	0.73	0.96	23.93 ± 0.02	14.17 ± 0.20	0.55 ± 0.02	8.89
NGC 2784 dw01	09:12:17.0	−24:12:47	15.38	0.83	0.99	23.54 ± 0.02	21.17 ± 0.31	0.74 ± 0.02	25.58
KK73	09:12:29.2	−24:14:28	14.45	0.82	1.08	21.90 ± 0.03	9.46 ± 0.30	1.26 ± 0.02	17.62
KSP-DW19	09:14:32.4	−23:33:26	15.26	0.53	0.73	22.68 ± 0.04	12.81 ± 0.39	0.94 ± 0.02	20.45
KSP-DW20	09:14:40.5	−24:15:10	17.74	0.71	0.89	23.82 ± 0.03	7.50 ± 0.26	0.84 ± 0.03	10.80
KSP-DW21	09:15:08.4	−25:02:58	20.15	0.79	0.88	23.87 ± 0.40	2.26 ± 0.81	0.97 ± 0.25	3.71
KSP-DW22	09:15:35.3	−23:48:57	17.57	0.33	0.64	23.47 ± 0.03	7.54 ± 0.23	0.72 ± 0.03	8.81
KSP-DW23	09:16:01.6	−23:36:23	20.47	24.33 ± 0.59	2.02 ± 1.24	1.15 ± 0.46	3.64
KSP-DW24	09:16:08.5	−23:43:17	18.11	0.72	0.83	24.04 ± 0.04	7.47 ± 0.30	0.75 ± 0.05	9.27
KSP-DW25	09:16:41.5	−23:06:08	20.19	0.47	1.21	24.75 ± 0.08	4.68 ± 0.24	0.46 ± 0.06	3.63
HIPASS J0916-23b	09:16:58.3	−23:16:45	14.08	0.33	0.57	20.78 ± 0.01	9.25 ± 0.18	0.93 ± 0.01	14.65
KSP-DW26	09:17:17.3	−24:22:05	19.83	0.42	1.03	24.80 ± 0.08	5.37 ± 0.32	0.57 ± 0.07	3.81
KSP-DW27	09:17:24.8	−22:33:42	18.48	1.18	1.16	25.04 ± 0.06	11.27 ± 0.44	0.56 ± 0.09	7.30
KSP-DW28	09:17:43.4	−23:29:37	16.64	0.49	0.74	23.18 ± 0.02	9.71 ± 0.19	0.78 ± 0.02	12.72
KSP-DW29	09:20:08.2	−25:00:06	19.19	0.67	0.87	23.61 ± 0.06	3.85 ± 0.20	0.70 ± 0.05	4.25
KSP-DW30	09:20:13.2	−23:56:02	18.11	0.61	0.54	24.37 ± 0.04	8.12 ± 0.33	0.85 ± 0.07	11.72
KSP-DW31	09:23:44.0	−23:03:57	19.39	0.71	0.62	24.57 ± 0.07	5.62 ± 0.34	0.66 ± 0.09	5.60

Notes.^a KSP-DW** candidates are newly discovered objects in KSP, while other names are from Karachentsev et al. (2013).^b *I* is *I*-band total magnitude derived from Sérsic fit.^c (*V* − *I*) and (*B* − *V*) are colors without the extinction correction.^d $\mu_{0,I}$, $r_{0,I}$, n_I , and $r_{e,I}$ are central surface brightness, scale length, curvature index, and effective radius derived for the *I*-band Sérsic fits, respectively.

incomplete. The number of member galaxies used for the fits vary from 16 (for the M106 group) to 55 (for the Local Group). The variation in number is in large part due to the more or less complete surveys of the relevant volumes, for example the survey area for M106 group extends only over $R < 0.13$ Mpc (Kim et al. 2011), and to the different detection limits for dwarf galaxies with very low surface brightness or compact size. Although the shape of the LF is not a function of the number of galaxies, many of the potential reasons for incompleteness in the surveys could translate differentially at different magnitudes. For example, in NGC 2784 we found that brighter dwarfs are more centrally concentrated, meaning that a survey that does not include the entire volume will be biased toward brighter dwarfs (see Figure 8). Likewise, incompleteness due to surface brightness effects will disfavor fainter galaxies. As such, it is extremely difficult to compare results from different

surveys, which will have different explicit and implicit selection criteria. A major strength of our eventually larger KMTNet survey of dwarf galaxies will be the homogeneity of the data and selection techniques. However, at the moment we can only compare results from various different surveys.

To search for a possible dependency of dwarf galaxy population with group properties, we investigate whether the faint-end slopes (α) of LFs of the six groups vary as a function of the group mass. We adopt two mass indicators (see Table 4): the total *K*-band luminosity of the group galaxies (L_K), which correlates with the group mass (Makarov & Karachentsev 2011), and the velocity dispersion derived from the radial velocities of the member galaxies in each group (σ_{group}). The galaxy luminosities and velocities are drawn from Karachentsev et al. (2013). We consider all galaxies associated with the same main disturber and $\Theta_1 > 0$ (tidal index) as members of

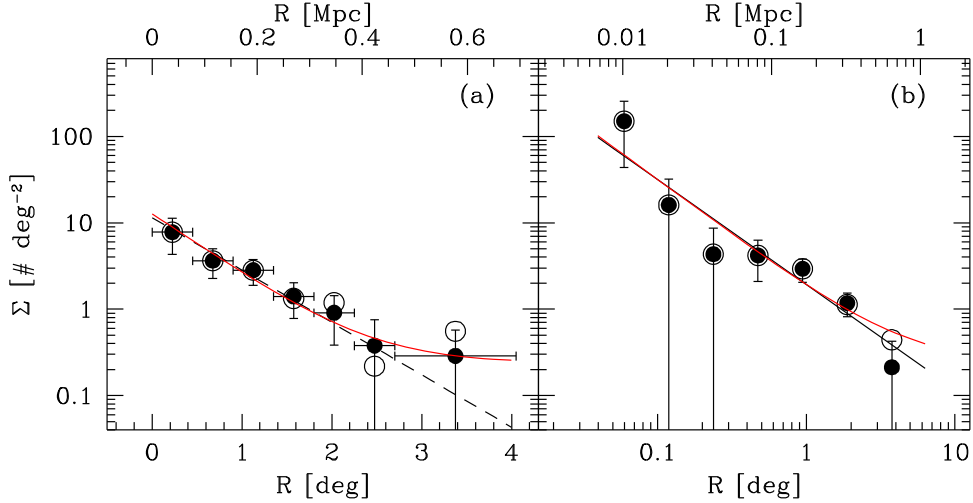


Figure 5. Radial number density of the dwarf galaxy candidates in the NGC 2784 field. The filled circles indicate the number densities obtained from the visually identified dwarf galaxies using only the region covered by deep stack images, while the open circles when using the region covered by both shallow and deep stacks. (a) The radial bin has equal linear interval except the last bin. The dashed line and solid curve indicate the exponential fit with $R \lesssim 3$ deg and the exponential function + constant fit, respectively. (b) The radial bin has equal logarithmic interval. The solid line and curve indicate the power law fits without and with constant value, respectively.

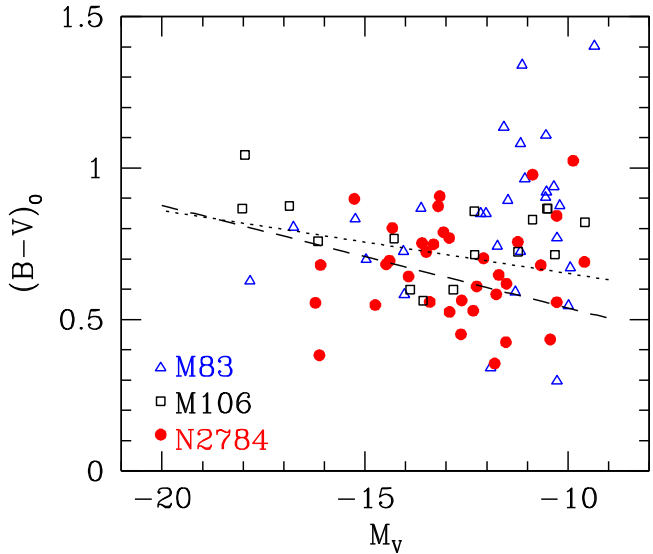


Figure 6. Color-magnitude diagram of the dwarf galaxy candidates in NGC 2784. The circles, triangles, and boxes represent the galaxy candidates in the NGC 2784 field (this study), M83 group (Müller et al. 2015), and M106 group (Kim et al. 2011), respectively. The dashed line denotes the color-magnitude relation obtained from the early-type galaxies in less-massive and less-dense Ursa Major cluster (Pak et al. 2014), while the dotted line from the early-type dwarf galaxies in more massive and more dense Virgo cluster (Lisker et al. 2008).

each group (see Karachentsev et al. (2013)). In Figure 11, we show the relationships between α and total luminosity or velocity dispersion. There is a mild suggestion in both plots that α decreases (shallower slope) as the mass of the galaxy group (L_K and σ_{group}) increases. When we simply fit the data with a linear function, we obtain $\alpha = 0.38 \log(L_K) - 5.47$ and $\alpha = 0.002\sigma_{\text{group}} - 1.447$. However, the correlation coefficient values (e.g., Pearson's r correlation, Spearman's rank correlation) estimated from the fits have approximately 1-sigma significance, and with this sample size statistical tests do not confirm this impression. In addition to the difficulty posed by

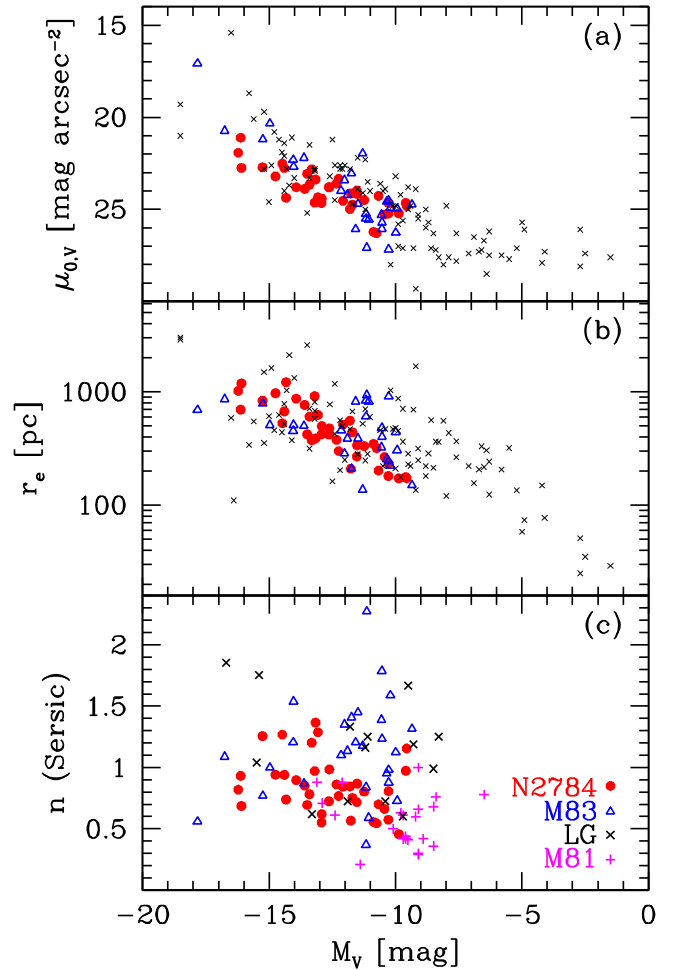


Figure 7. Central surface brightness (a), effective radius (b), and Sérsic n (c) vs. total absolute magnitudes of the dwarf galaxies. The circles, triangles, crosses, and pluses indicate the dwarfs in the NGC 2784 field (this study), M83 group (Müller et al. 2015), the Local Group (McConnachie (2012) for μ_0 , r_e and Jerjen et al. (2000) for Sérsic n), and M81 group (Chiboucas et al. 2009), respectively.

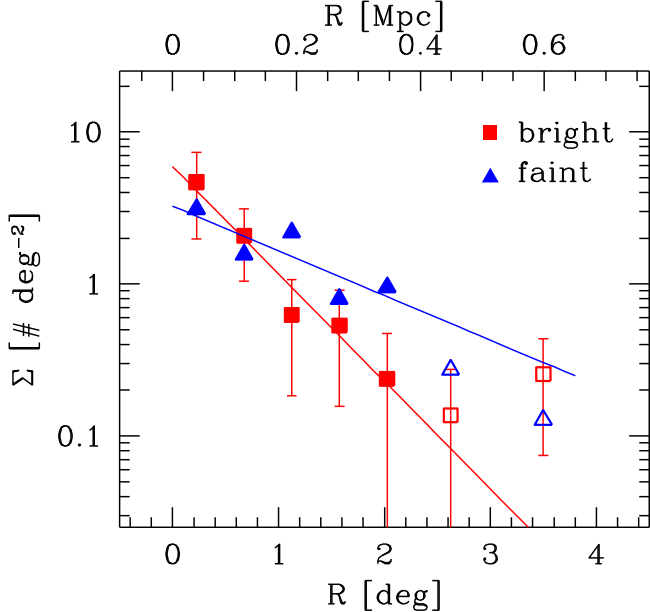


Figure 8. Radial number density of the dwarf galaxy candidates in the NGC 2784 field. The boxes and triangles are the bright ($M_V < -13$) and faint ($M_V \geq -13$) dwarfs, respectively. The solid lines represent exponential fits to each of the group. The filled and open symbols indicate inner and outer samples divided at $R \approx 2.5$, respectively. The filled symbols, mostly derived from the deep stack images, are used to get the fits.

the small statistical sample, we are concerned about systematic effects resulting from the comparison of results from diverse surveys. While intriguing, this test needs to be revisited once a large and uniform survey is completed. Our KMTNet survey of 15–20 groups should be well positioned to address this topic.

5. Summary

Using deep, wide-field images obtained from the KMTNet Supernova Program, we identified 38 dwarf galaxy candidates, 31 of which were previously unknown, in the nearby NGC 2784 galaxy group and measured their photometric properties. KMTNet survey data produce competitive dwarf galaxy surveys to the current state-of-the-art. Our primary results are summarized as follows.

1. We discovered 31 dwarf galaxy candidates around NGC 2784 galaxy over 30 sq. deg.. Based on their cluster around NGC 2784, we estimate that at least 85% of these are physically associated with the NGC 2784 group. Beyond a projected separation of 0.5 Mpc, the number density profile flattens and we may be detecting only field contaminants.
2. We present surface photometry for 38 dwarfs, our new discoveries, plus the previously known seven dwarf galaxies (Karachentsev et al. 2013). Our 3σ surface brightnesses limit is approximately $\mu_V \sim 28.5$ mag arcsec $^{-2}$. The central surface brightness and total absolute magnitude of the faintest dwarf galaxies we detect are $\mu_{0,V} \sim 26.1$ mag arcsec $^{-2}$ and $M_V \sim -9.5$ mag, respectively. The effective radii of the dwarfs are all larger than ~ 3.5 arcsec (~ 170 pc at the distance of NGC 2784).

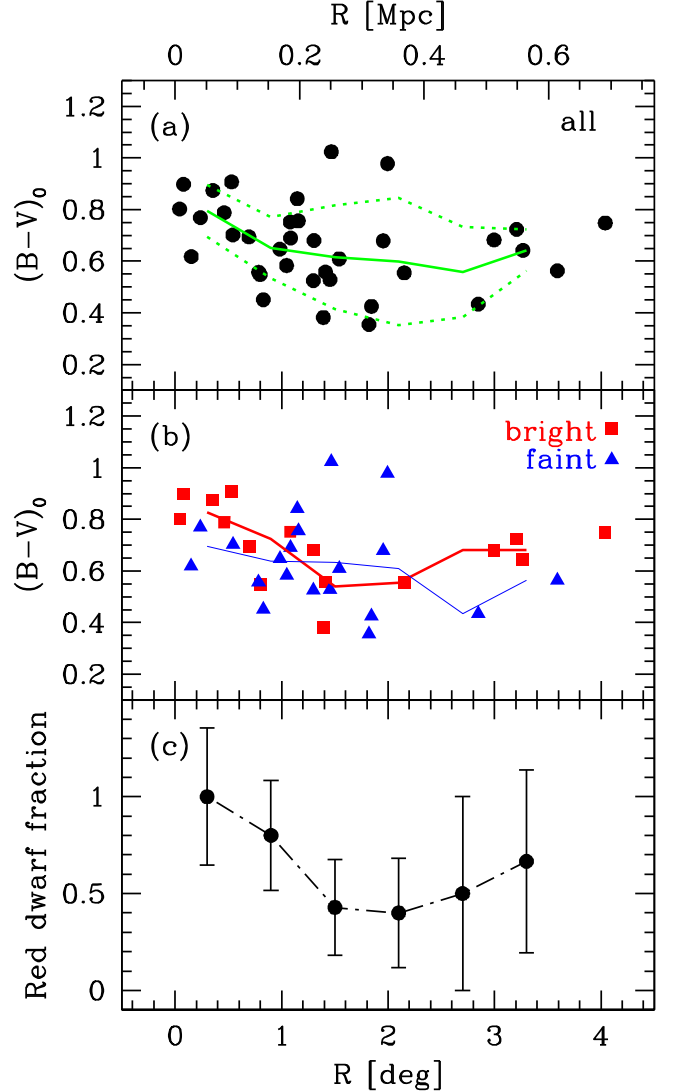


Figure 9. Radial color distributions ((a) and (b)) and red dwarf fraction (c) of the dwarf galaxy candidates in the NGC 2784 field. The solid and dotted curves indicate the mean color values and standard deviation in each radial bin, respectively. The circles, boxes, and triangles represent all, bright ($M_V < -13$), and faint ($M_V \geq -13$) dwarf samples, respectively. The errors of red dwarf fraction are estimated by assuming a Poisson distribution.

3. The radial number density of the dwarf candidates decreases exponentially (or with power index, $\alpha \approx -1.3$) with distance from the center of NGC 2784. The background contamination is about 15%, so we estimate that about 27 of the 32 candidates within 2.7 degree are dwarf members of the group.
4. The color and Sérsic structural parameters for the dwarf candidates are consistent with those of dwarfs in other galaxy groups (M81, M83, M106, and the Local Group). The dwarf galaxy candidates have a color–magnitude relation similar to that of early-type galaxies.
5. The color and number density radial profiles for the candidate dwarf population in the NGC 2784 group galaxies, shows that the central dwarfs are both brighter and redder than the rest of the population. We caution that contamination is likely to produce relations of the

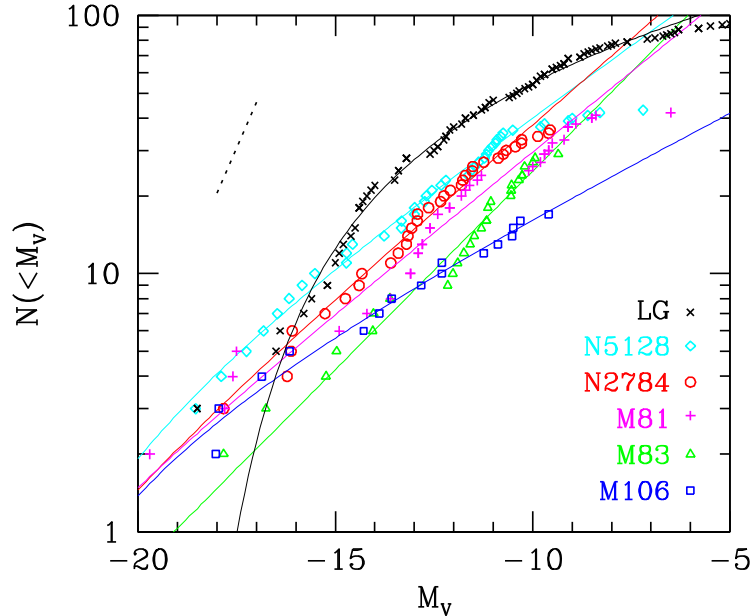


Figure 10. Cumulative luminosity function of galaxies in several galaxy groups. The crosses, diamonds, circles, pluses, triangles, and boxes represent the galaxies in the Local Group (McConnachie 2012; Martin et al. 2013a, 2013b), NGC 5128 group (Tully et al. 2015; Crnojević et al. 2016), NGC 2784 group (this study), M81 group (Chiboucas et al. 2009), M83 group (Müller et al. 2015), and M106 group (Kim et al. 2011), respectively. The solid lines indicate the best fitting Schechter function on each data. The dotted line represents the faint-end slope ($\alpha = -1.8$) of halo mass expected from the Λ CDM model (Trentham & Tully 2002).

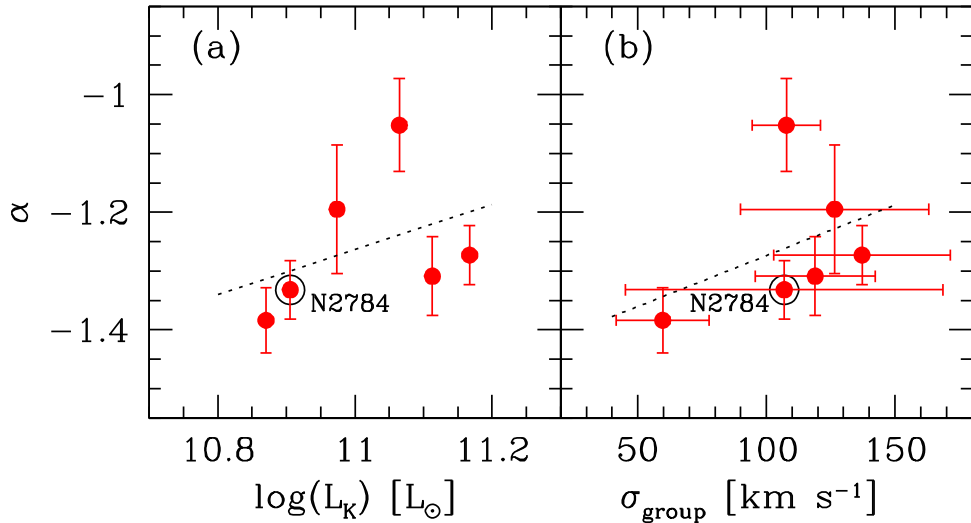


Figure 11. Luminosity function slopes of the dwarf galaxies in the galaxy groups as a function of (a) the total K -band luminosity of the groups (L_K) and (b) the velocity dispersion of the member galaxies in each group (σ_{group}). The filled circles with the large open circle indicate the measurement of the NGC 2784 group obtained in this study and the other filled circles are those of other groups obtained from the literature data. The dotted lines represent the linear least-square fits to the data.

Table 4
Faint-end Slopes of the Luminosity Function of Galaxy Groups

Group	α	$\log L_K$ (L_\odot)	σ_{group} (km s^{-1})
M83	-1.39 ± 0.05	10.87	60 ± 18
NGC 2784	-1.33 ± 0.05	10.91	107 ± 61
M106	-1.20 ± 0.10	10.97	127 ± 36
Local Group	-1.05 ± 0.08	11.07	108 ± 13
M81	-1.31 ± 0.06	11.11	119 ± 23
NGC 5128	-1.27 ± 0.05	11.17	137 ± 34

same sense, but argue that the results are not dominated by the contamination.

- The faint-end slope of the LF of the NGC 2784 group galaxies is $\alpha \approx -1.33 \pm 0.05$, which is consistent with that seen in some other groups, but apparently steeper than that of the Local Group galaxies. Eventually, the KMTNet survey will provide homogeneous catalogs of dwarf galaxies in 15–20 groups.

The authors are grateful to the staffs of the KMTNet. Drs. Youngdae Lee and Suk Kim are thanked for their useful

comments. This research has made use of the KMTNet system operated by the Korea Astronomy and Space Science Institute (KASI), and the data were obtained at three host sites of CTIO in Chile, SAAO in South Africa, and SSO in Australia.

ORCID iDs

- Hong Soo Park <https://orcid.org/0000-0002-3505-3036>
 Dae-Sik Moon <https://orcid.org/0000-0003-4200-5064>
 Dennis Zaritsky <https://orcid.org/0000-0002-5177-727X>
 Jae-Joon Lee <https://orcid.org/0000-0003-0894-7824>
 Dong-Jin Kim <https://orcid.org/0000-0002-7038-2118>

References

- APASS 2015, The AAVSO Photometric All-Sky Survey: Data Release 9, <https://www.aavso.org/apass/>
- Bechtol, K., Drlica-Wagner, A., Balbinot, E., et al. 2015, *ApJ*, 807, 50
- Behroozi, P. S., Conroy, C., & Wechsler, R. H. 2010, *ApJ*, 717, 379
- Benson, A. J., Lacey, C. G., Baugh, C. M., Cole, S., & Frenk, C. S. 2002, *MNRAS*, 333, 156
- Bertin, E. 2006, in ASP Conf. Ser. 351, Automatic Astrometric and Photometric Calibration with SCAMP, ed. C. Gabriel et al. (San Francisco, CA: ASP), 112
- Bertin, E., & Arnouts, S. 1996, *A&AS*, 317, 393
- Bertin, E., Mellier, Y., Radovich, M., et al. 2002, in ASP Conf. Ser. 281, The TERAPIX Pipeline, ed. D. A. Bohlender, D. Durand, & T. H. Handley (San Francisco, CA: ASP), 228
- Chiboucas, K., Karachentsev, I. D., & Tully, R. B. 2009, *AJ*, 137, 3009
- Cooper, A. P., Cole, S., Frenk, C. S., et al. 2010, *MNRAS*, 406, 744
- Crnojević, D., Sand, D. J., Spekkens, K., et al. 2016, *ApJ*, 823, 19
- Doyle, M. T., Drinkwater, M. J., Rohde, D. J., et al. 2005, *MNRAS*, 361, 34
- Drlica-Wagner, A., Bechtol, K., Rykoff, E. S., et al. 2015, *ApJ*, 813, 109
- Ferrarese, L., Côté, P., Jordán, A., et al. 2006, *ApJS*, 164, 334
- Ferrarese, L., Côté, P., Sánchez-Janssen, R., et al. 2016, *ApJ*, 824, 10
- Fisher, J. R., & Tully, R. B. 1981, *ApJS*, 47, 139
- Fouque, P., Gourgoulhon, E., Chamaraux, P., & Paturel, G. 1992, *A&AS*, 93, 211
- Garcia, A. M. 1993, *A&AS*, 100, 47
- He, M. Y., Moon, D.-S., Neilson, H., et al. 2016, *JKAS*, 49, 209
- Jerjen, H., Binggeli, B., & Freeman, K. C. 2000, *AJ*, 119, 593
- Karachentsev, I. D., Makarov, D. I., & Kaisina, E. I. 2013, *AJ*, 145, 101
- Karachentsev, I. D., Makarov, D. I., Karachentseva, V. E., & Melnik, O. V. 2008, *AstL*, 34, 832
- Kim, E., Kim, M., Hwang, N., et al. 2011, *MNRAS*, 412, 1881
- Kim, S.-L., Lee, C.-U., Park, B.-G., et al. 2016, *JKAS*, 49, 37
- Klypin, A., Kravtsov, A. V., Valenzuela, O., & Prada, F. 1999, *ApJ*, 522, 82
- Lee, Y., Rey, S.-C., Hilker, M., Sheen, Y.-K., & Yi, S. K. 2016, *ApJ*, 822, 92
- Lisker, T., Grebel, E. K., & Binggeli, B. 2008, *AJ*, 135, 380
- Lisker, T., Weinmann, S. M., Janz, J., & Meyer, H. T. 2013, *MNRAS*, 432, 1162
- Lupton, R. 2005, Transformations between SDSS magnitudes and other systems, <https://www.sdss3.org/dr10/algorithms/sdssUBVRITransform.php/>
- Makarov, D., & Karachentsev, I. 2011, *MNRAS*, 412, 2498
- Markwardt, C. B. 2009, in ASP Conf. Ser. 411, Astronomical Data Analysis Software and Systems XVIII, ed. D. A. Bohlender, D. Durand, & P. Dowler (San Francisco, CA: ASP), 251
- Martin, N. F., Schlafly, E. F., Slater, C. T., et al. 2013a, *ApJL*, 779, L10
- Martin, N. F., Slater, C. T., Schlafly, E. F., et al. 2013b, *ApJ*, 772, 15
- McConnachie, A. W. 2012, *AJ*, 144, 4
- McConnachie, A. W., Irwin, M. J., Ibata, R. A., et al. 2009, *Natur*, 461, 66
- Merritt, A., van Dokkum, P., & Abraham, R. 2014, *ApJL*, 787, L37
- Moon, D.-S., Kim, S. C., Lee, J.-J., et al. 2016, *Proc. SPIE*, 9906, 99064I
- Moore, B., Ghigna, S., Governato, F., et al. 1999, *ApJL*, 524, L19
- Müller, O., Jerjen, H., & Binggeli, B. 2015, *A&A*, 583, A79
- Müller, O., Jerjen, H., & Binggeli, B. 2017, *A&A*, 597, A7
- Muñoz, R. P., Egenthaler, P., Puzia, T. H., et al. 2015, *ApJL*, 813, L15
- Pak, M., Rey, S.-C., Lisker, T., et al. 2014, *MNRAS*, 445, 630
- Popesso, P., Biviano, A., Böhringer, H., & Romaniello, M. 2006, *A&A*, 445, 29
- Presotto, V., Iovino, A., Scodéglio, M., et al. 2012, *A&A*, 539, A55
- Roberts, I. D., Parker, L. C., Joshi, G. D., & Evans, F. A. 2015, *MNRAS*, 448, L1
- Schechter, P. 1976, *ApJ*, 203, 297
- Schlafly, E. F., & Finkbeiner, D. P. 2011, *ApJ*, 737, 103
- Smith, R. J., Lucey, J. R., Price, J., Hudson, M. J., & Phillipps, S. 2012, *MNRAS*, 419, 3167
- Sprinthall, R. C. 2011, Basic Statistical Analysis (9th ed.; Old Tappan, NJ: Pearson Education)
- Tonry, J. L., Dressler, A., Blakeslee, J. P., et al. 2001, *ApJ*, 546, 681
- Trentham, N., & Tully, R. B. 2002, *MNRAS*, 335, 712
- Trentham, N., & Tully, R. B. 2009, *MNRAS*, 398, 722
- Tully, R. B., Libeskind, N. I., Karachentsev, I. D., et al. 2015, *ApJL*, 802, L25
- Weinmann, S. M., Lisker, T., Guo, Q., Meyer, H. T., & Janz, J. 2011, *MNRAS*, 416, 1197
- Wetzel, A. R., Tinker, J. L., & Conroy, C. 2012, *MNRAS*, 424, 232
- Wetzel, A. R., Tinker, J. L., Conroy, C., & van den Bosch, F. C. 2013, *MNRAS*, 432, 336